

## HYDRODYNAMIC COUPLING OF VISCOUS AND NON-VISCOUS NUMERICAL WAVE SOLUTIONS WITHIN THE OPEN-SOURCE HYDRODYNAMICS FRAMEWORK REEF3D

**Weizhi Wang** \*  
Department of Civil and  
Environmental Engineering  
NTNU  
7491 Trondheim, Norway  
Email: weizhi.wang@ntnu.no

**Csaba Pákozdi**  
Ships and Ocean Structures  
SINTEF Ocean  
7465 Trondheim, Norway

**Arun Kamath**  
**Tobias Martin**  
**Hans Bihs**  
Department of Civil and  
Environmental Engineering  
NTNU  
7491 Trondheim, Norway

### ABSTRACT

A comprehensive understanding of the marine environment in the offshore area requires phase-resolved wave information. For the far-field wave propagation, computational efficiency is crucial, as large spatial and temporal scales are involved. For the near-field extreme wave events and wave impacts, high resolution is required to resolve the flow details and turbulence. The combined use of a computationally efficient large-scale model and a high-resolution local-scale solver provides a solution that combines accuracy and efficiency. This article introduces a coupling strategy between the efficient fully nonlinear potential flow (FNPF) solver REEF3D::FNPF and the high-fidelity computational fluid dynamics (CFD) model REEF3D::CFD within the open-source hydrodynamics framework REEF3D. REEF3D::FNPF solves the Laplace equation together with the boundary conditions on a sigma-coordinate. The free surface boundary conditions are discretised using high-order finite difference methods. The Laplace equation for the velocity potential is solved with a conjugated gradient solver preconditioned with geometric multi-grid provided by the open-source library hypre. The model is fully parallelised following the domain decomposition strategy and the MPI protocol. The waves calculated with the FNPF solver are used as wave genera-

tion boundary condition for the CFD based numerical wave tank REEF3D::CFD. The CFD model employs an interface capturing two-phase flow approach that can resolve complex wave structure interaction, including breaking wave kinematics and turbulent effects. The presented hydrodynamic coupling strategy is tested for various wave conditions and the accuracy is fully assessed.

### INTRODUCTION

In the last decade, the use of computational fluid dynamics (CFD) based numerical wave tanks (NWT) for the simulation of wave hydrodynamics has been significantly increasing. Prominent examples of this development are the papers by Jacobsen et al [1] which introduced the wave generation toolbox waves2foam to OpenFOAM and Higuera et al. [2] which presented a similar modification to the open-source CFD model as well. Several commercial CFD codes exist which offer the capability to generate waves, such as for example StarCCM+ [3] [4].

Another NWT that solves the Navier-Stokes equations is REEF3D, which employs the level set method for the free surface together with high-order discretization schemes [5]. These type of models share the idea of solving wave hydrodynamics as two phase flow together with interface capturing. With this approach, the free surface can be deformed beyond the point of

\*Address all correspondence to this author.

breaking and demanding wave problems can be solved. Examples are breaking wave interaction with monopiles [6], complex structures [7] and strong deformations of the free surface to due the impact of moving solid structures [8].

Some of the advantages of the CFD based NWTs are their ability to resolve the complex free surface under breaking waves as well as considering viscous effects. On the other hand, for pure wave propagation over long distances with or without breaking, they can be less than ideal as the grid and time step requirements lead to relatively high use of computational resources. For wave propagation in wave tanks or wave basins away from structures, the effects of wave breaking need to be accounted for but are not required to be fully resolved as is the case around structures where the breaking wave impact leads to significantly increased wave forces. Instead, the effect of the breaking waves can be incorporated through a modification of the wave kinematics mimicking the energy dissipation that takes place in the breaking process. As a consequence, an efficient one-phase potential flow solver is an attractive option for the phase-resolved far-field wave solution. In several papers, Engsig-Karup et al. have highlighted the possibilities of finite differences based fully-nonlinear potential flow models, see e.g. [9] [10] [11], a type of wave model first introduced by [12]. More recently, a fully-nonlinear potential flow (FNPF) model was incorporated in the open-source hydrodynamics suite REEF3D [13] [14]. REEF3D::FNPF makes use of the high-order spatial and temporal discretization schemes and the high-performance capabilities for parallel computing available in this framework.

The idea is to utilize each model to their advantage, i.e. employing the potential flow solver for the far-field, while resolving the breaking wave with a two-phase flow CFD solver. Paulsen et al. [15] have shown the possibility of coupling OceanWave3D with OpenFOAM for focused breaking wave impact with a cylindrical structure. Baquet et al. [16] combined the in-house potential flow solver TPNWT with the commercial CFD software StarCCM+ for three-hour irregular wave simulations in a two-dimensional wave tank.

In most previous studies, the potential flow solver and the CFD solver are often provided by different developers. This requires the engineers to understand the numerical architecture of both models and the interface between the solvers tends to be more challenging. In this paper, the different solvers of the same open-source hydrodynamics software REEF3D are coupled, REEF3D:FNPF for the non-linear wave propagation and REEF3D:CFD for the breaking wave modeling. Since both solvers are part of the same numerical framework, the numerics are more consistent and the coupling interface can be more robust and straightforward. For most practical purposes, only one-way coupling is required where the potential flow solution prescribes the wave boundary condition in the viscous solver. At first, a validation study is performed for a two-dimensional numerical

wave tank with regular waves. Here, the numerical results are compared with analytical wave solutions. Then, breaking waves over a submerged reef [17] are calculated. The numerical results for the breaking wave case are compared with experimental data from large-scale wave flume experiments.

## NUMERICAL MODEL

### REEF3D::FNPF

The fully non-linear potential flow model REEF3D::FNPF is based on the idea of using finite difference discretization schemes on three-dimensional grids. Several simplifications are made, such as inviscid, irrotational and incompressible flow, and as such the governing equation for the flow is the Laplace equation:

$$\frac{\partial^2 \Phi}{\partial x^2} + \frac{\partial^2 \Phi}{\partial y^2} + \frac{\partial^2 \Phi}{\partial z^2} = 0 \quad (1)$$

As an elliptic equation, the Laplace equation for the flow potential is fully governed by the boundary conditions, which are required on all domain boundaries for the velocity potential  $\Phi$ . Simple Neuman boundary conditions are used at walls or inflow wave generation (non-relaxation zone type). Kinematic boundary conditions for the potential are required at the bed, where the fluid particle cannot penetrate the solid boundary:

$$\frac{\partial \Phi}{\partial z} + \frac{\partial h}{\partial x} \frac{\partial \Phi}{\partial x} + \frac{\partial h}{\partial y} \frac{\partial \Phi}{\partial y} = 0, \quad z = -h. \quad (2)$$

The boundary conditions at the free surface require special attention. The fluid particles should remain at the free surface at the same time as the pressure at the free surface is equal to the atmospheric pressure. Resulting from this, the kinematic free surface boundary condition for the free surface elevation  $\eta$  are formulated [12]:

$$\frac{\partial \eta}{\partial t} = - \frac{\partial \eta}{\partial x} \frac{\partial \tilde{\Phi}}{\partial x} - \frac{\partial \eta}{\partial y} \frac{\partial \tilde{\Phi}}{\partial y} + \tilde{w} \left( 1 + \left( \frac{\partial \eta}{\partial x} \right)^2 + \left( \frac{\partial \eta}{\partial y} \right)^2 \right), \quad (3)$$

For the free surface velocity potential  $\tilde{\Phi}$ , the dynamic free

surface boundary condition is defined as:

$$\begin{aligned} \frac{\partial \tilde{\Phi}}{\partial t} = & -\frac{1}{2} \left( \left( \frac{\partial \tilde{\Phi}}{\partial x} \right)^2 + \left( \frac{\partial \tilde{\Phi}}{\partial y} \right)^2 \right) \\ & + \frac{1}{2} \tilde{w}^2 \left( 1 + \left( \frac{\partial \eta}{\partial x} \right)^2 + \left( \frac{\partial \eta}{\partial y} \right)^2 \right) - g\eta. \end{aligned} \quad (4)$$

where  $\mathbf{x} = (x, y)$  represents the horizontal location and  $\tilde{w}$  is the vertical velocity at the free surface.

With the boundary conditions in place, the Laplace equation is then solved with a finite difference scheme on a  $\sigma$ -coordinate grid. The Laplace equation is solved with the conjugated gradient BiCGStab solver [18] preconditioned with the geometric multigrid solver PFMG [19] provided by the open-source linear solver library hypre. The  $\sigma$ -coordinate is transferred from a Cartesian grid following:

$$\sigma = \frac{z + h(\mathbf{x})}{\eta(\mathbf{x}, t) + h(\mathbf{x})} \quad (5)$$

Through the sigma coordinate transformation, the velocities can be calculated as follows, once the velocity potential  $\Phi$  is obtained:

$$u(\mathbf{x}, z) = \frac{\partial \Phi(\mathbf{x}, z)}{\partial x} = \frac{\partial \Phi(\mathbf{x}, \sigma)}{\partial x} + \frac{\partial \sigma}{\partial x} \frac{\partial \Phi(\mathbf{x}, \sigma)}{\partial \sigma}, \quad (6)$$

$$v(\mathbf{x}, z) = \frac{\partial \Phi(\mathbf{x}, z)}{\partial y} = \frac{\partial \Phi(\mathbf{x}, \sigma)}{\partial y} + \frac{\partial \sigma}{\partial y} \frac{\partial \Phi(\mathbf{x}, \sigma)}{\partial \sigma}, \quad (7)$$

$$w(\mathbf{x}, z) = \frac{\partial \sigma}{\partial z} \frac{\partial \Phi(\mathbf{x}, \sigma)}{\partial \sigma}. \quad (8)$$

The waves are generated at the wave generation zone using the relaxation method [20], as shown in Eqn. (9). In the wave generation zone, the free-surface elevation and velocities are ramped up to the designed theoretical values. At the numerical beach for the numerical wave tank without structures, a reverse process takes place and the flow properties are restored to hydrostatic values following the relaxation method using an improved relaxation function [21]. For the cases where breaking occurs, the post-breaking waves are absorbed with active wave absorption [22].

$$\Gamma(\tilde{x}) = 1 - \frac{e^{(\tilde{x}^{3.5})} - 1}{e - 1} \text{ for } \tilde{x} \in [0; 1] \quad (9)$$

where  $\tilde{x}$  is scaled to the length of the relaxation zone.

The spatial discretization of the free surface elevation and velocity potential in the kinematic and dynamics free surface boundary conditions are solved with the fifth-order WENO (weighted essentially non-oscillatory) scheme [23]. This scheme can handle large gradients accurately by considering the local smoothness and weighting the different ENO stencils accordingly, with the smoothest stencil assigned the largest weights. For the time treatment, a third-order accurate TVD Runge-Kutta scheme [24] is used. Adaptive time stepping is used in order to determine the time step size while keeping a constant CFL number which is based on phase velocity. The model is fully parallelized following the domain decomposition strategy, employing parallel communication via MPI (Message Passing Interface).

### REEF3D::CFD

The incompressible fluid flow is described by the three-dimensional Reynolds-Averaged Navier-Stokes equations (RANS), which are solved together with the continuity equation for prescribing momentum and mass conservation: The viscous fluid solver REEF3D::CFD calculates the wave field using the continuity and Navier-Stokes equations as governing equations:

$$\frac{\partial u_i}{\partial x_i} = 0 \quad (10)$$

$$\frac{\partial u_i}{\partial t} + u_j \frac{\partial u_i}{\partial x_j} = -\frac{1}{\rho} \frac{\partial p}{\partial x_i} + \frac{\partial}{\partial x_j} \left[ (v + \nu_t) \left( \frac{\partial u_i}{\partial x_j} + \frac{\partial u_j}{\partial x_i} \right) \right] + g_i \quad (11)$$

where  $u$  is the velocity averaged over time  $t$ ,  $\rho$  is the fluid density,  $p$  is the pressure,  $\nu$  is the kinematic viscosity,  $\nu_t$  is the eddy viscosity and  $g$  the acceleration due to gravity.

In the current paper Reynolds-Averaging is performed and consequently, the the eddy viscosity  $\nu_t$  in the RANS equations is calculated through the two-equation  $k$ - $\omega$  model [25]. This turbulence model consists of the two equations for the turbulent kinetic energy  $k$  and the specific turbulent dissipation  $\omega$ :

$$\frac{\partial k}{\partial t} + u_j \frac{\partial k}{\partial x_j} = \frac{\partial}{\partial x_j} \left[ \left( \nu + \frac{\nu_t}{\sigma_k} \right) \frac{\partial k}{\partial x_j} \right] + P_k - \beta_k k \omega \quad (12)$$

$$\frac{\partial \omega}{\partial t} + u_j \frac{\partial \omega}{\partial x_j} = \frac{\partial}{\partial x_j} \left[ \left( \nu + \frac{\nu_t}{\sigma_\omega} \right) \frac{\partial \omega}{\partial x_j} \right] + \frac{\omega}{k} \alpha P_k - \beta \omega^2 \quad (13)$$

where  $P_k$  is the turbulent production rate, the empirical coefficients are defined as  $\alpha = \frac{5}{9}$ ,  $\beta_k = \frac{9}{100}$ ,  $\beta = \frac{3}{40}$ ,  $\sigma_k = 2$  and  $\sigma_\omega = 2$ .

At the free surface, the turbulent length-scales are suppressed, in effect dissipation turbulent kinetic energy [26]. As this physical phenomena is not directly incorporated in the  $k-\omega$  model, the specific turbulent dissipation at the free surface needs to be defined as shown and validated in [5] and [27]:

$$\omega_s = \frac{c_\mu^{-\frac{1}{4}}}{\kappa} k^{\frac{1}{2}} \cdot \left( \frac{1}{y'} + \frac{1}{y^*} \right) \quad (14)$$

where  $c_\mu = 0.07$  and  $\kappa = 0.4$ . The variable  $y'$  is the virtual origin of the turbulent length scale, and was empirically found to be 0.07 times the mean water depth [28].

The pressure as the driving force of the fluid flow is modeled with Chorin's projection method [29] for incompressible fluids. Following this strategy, the pressure gradient is removed from the momentum equations in the first step. The updated velocity after each Euler step of the time discretization is the intermediate velocity  $U_i^*$ . The Poisson equation for pressures is formed by calculating the divergence of the intermediate velocity field:

$$-\frac{\partial}{\partial x_i} \left( \frac{1}{\rho(\phi^n)} \frac{\partial p}{\partial x_i} \right) = -\frac{1}{\Delta t} \frac{\partial u_i^*}{\partial x_i} \quad (15)$$

As the Laplace equation in REEF3D::FNPF, the Poisson equation is solved with hypre's conjugated gradient BiCGStab solver [18] preconditioned with the geometric multigrid solver PFMG. The new pressure corrects the velocity field, making it divergence free. The convective terms of the RANS equations are discretized with the fifth-order WENO scheme [23] in the conservative finite-difference framework. For the time treatment of the momentum and the level set equations, a third-order accurate TVD Runge-Kutta scheme is employed, consisting of three Euler steps [24].

$$\begin{aligned} \phi^{(1)} &= \phi^n + \Delta t L(\phi^n) \\ \phi^{(2)} &= \frac{3}{4}\phi^n + \frac{1}{4}\phi^{(1)} + \frac{1}{4}\Delta t L(\phi^{(1)}) \\ \phi^{n+1} &= \frac{1}{3}\phi^n + \frac{2}{3}\phi^{(2)} + \frac{2}{3}\Delta t L(\phi^{(2)}) \end{aligned} \quad (16)$$

All variables are solved on a Cartesian mesh, ensuring tight velocity pressure coupling. In case of solid structures, an immersed boundary method is used through the implementation of ghost cells [30].

The free surface is captured with the level set function [31], which is defined as a signed distance function:

$$\phi(\vec{x}, t) \begin{cases} > 0 \text{ if } \vec{x} \in \text{phase 1} \\ 0 \text{ if } \vec{x} \in \Gamma \\ < 0 \text{ if } \vec{x} \in \text{phase 2} \end{cases} \quad (17)$$

The Eikonal equation  $|\nabla\phi| = 1$  is valid, ensuring that the distance function property is achieved. The level set function is coupled with the flow solver through the convection equation for the level set function:

$$\frac{\partial \phi}{\partial t} + u_j \frac{\partial \phi}{\partial x_j} = 0 \quad (18)$$

The convection term in Eq. (18) is solved with the Hamilton-Jacobi version of the WENO scheme [32]. For time stepping, the third-order TVD Runge-Kutta scheme is used [24]. In order to continuously maintain the signed distance property and mass conservation, a PDE based reinitialization equation is solved [33]:

$$\frac{\partial \phi}{\partial t} + S(\phi) \left( \left| \frac{\partial \phi}{\partial x_j} \right| - 1 \right) = 0 \quad (19)$$

where  $S(\phi)$  is the smoothed sign function [34].

## Hydrodynamic Coupling

In this paper, a one-way hydrodynamic coupling (HDC) approach is presented. The velocities and free surface elevation from the non-viscous potential flow solver are transferred to the viscous solver. In the process, the grid generator DIVEMesh in the open-source hydrodynamic framework REEF3D is used to interpolate the flow information stored in the  $\sigma$ -grid from the non-viscous solver to the Cartesian grid in the viscous CFD solver. A linear interpolation scheme is applied in the current studies. After the flow information is collected and interpolated, DIVEMesh decomposes the computational domain from the N1, the number of sub-domains in the non-viscous potential flow region, to N2, the new number of sub-domains to be used in the CFD domain. This allows for flexible combinations of parallel computations in the non-viscous and viscous domains. A coupling zone following the relaxation method is arranged at the inlet boundary of the CFD domain to initialise the flow information obtained from the non-viscous model and propagate waves to its computational domain. The pressure field is, however, not

prescribed in the coupling zone inside the CFD domain. Similarly, the velocity field in the air phase in the CFD domain is not prescribed. The hydrodynamic pressure and the air velocities are calculated automatically in the CFD domain using the given flow information from the non-viscous model. This reduces the sensitivity at the coupling boundary in the CFD domain while maintaining accuracy.

A flow chart that summarises the HDC process in REEF3D is presented in Fig. 1.

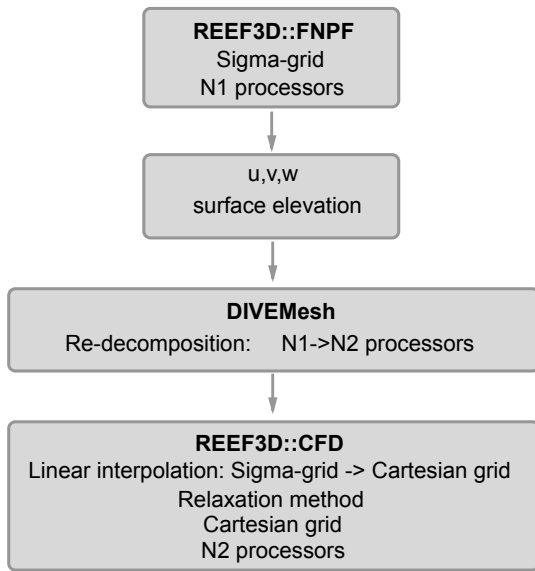


**FIGURE 1:** Hydrodynamic coupling (HDC) procedure implemented in REEF3D.

## RESULTS

### Empty Wave Tank

In the first step, the hydrodynamic coupling procedure is tested with a two-dimensional (2D) wave propagation over constant water depth. A 2nd-order Stokes wave with a wave height of 0.1 m and a wave length of 4 m over a water depth of 2 m is generated in the fully nonlinear potential flow solver REEF3D::FNPF. The numerical wave tank of the potential flow domain is 100 m long in the direction of wave propagation. A one-wavelength wave generation (WG) zone using the relaxation method is located at the inflow boundary and a two-wavelength numerical beach (NB) is arranged at the outflow boundary. The CFD domain starts from  $X_c = 60$  m, where the hydrodynamic coupling takes place, until the end of the numerical wave tank.

As a result, the CFD domain is only 40 m long in the wave propagation direction. A one-wavelength hydrodynamic coupling zone is used to initialise the flow information from the potential flow model following the relaxation method used in the wave generation zone. The potential flow model simulates 200 s wave propagation while the CFD model obtains the flow information from  $t_c = 100$  s and simulates the wave propagation for 80 s. The schematics of the numerical wave tank set-up for the FNPF domain and the CFD domain is illustrated in Fig. 2.

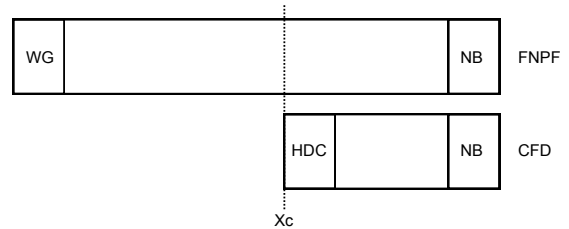


**FIGURE 2:** Schematics of the numerical wave tank set-up of the FNPF and the CFD domains for the simulation of wave propagation over constant water depth. WG stands for the wave generation zone, NB is the numerical beach, HDC represents the hydrodynamic coupling zone between the models and  $X_c$  is the location where the coupling procedure and the CFD domain starts.

In the potential flow domain, the horizontal cell size is 0.1 m and 12 cells are arranged in the vertical direction. The 200 s simulated is performed with 4 processors (2.7GHz Intel Xeon E5) for 231 s. In the CFD simulation, a uniform cell size of 0.04 m is used. The 80 s simulation takes 1588.6 s in the CFD domain with 12 processors of the same type. The simulated time history of the free surface elevation in the potential flow domain and the HDC domain are compared at the coupling boundary at  $x = 60$  m and near the end of the wave tank at  $x = 90$  m, as shown in Fig. 3.

It is seen that both the potential flow simulation and the HDC simulation produce high quality wave field that match the wave phase as well as wave amplitude provide by the wave theory. The surface elevation time history in the CFD domain overlaps with the FNPF domain, indicating little error in the coupling process.

However, the coupling process might be sensitive to the configuration of the coupling zone. In the following test, different  $L_c$ , length of the coupling zone, are investigated. The surface elevation time histories at  $x = 90$  m are compared with  $L_c = 0.25\lambda, 0.5\lambda, \lambda$  and  $2\lambda$ , where  $\lambda$  is the wavelength. The comparison is shown in Fig. 4. It is seen that the wave phase is shifted when only 0.25 wavelength is used for the coupling zone and the wave amplitude is amplified when 0.5 wavelength is used. In order to obtain an accurate representation of the wave

propagation, at least one wavelength is required for the coupling zone.

### Breaking Wave

One of the limitations of non-viscous models is the lack of ability to represent strong overturning breaking waves. In this case, only viscous CFD models are able to capture the complicated overturning wave crest geometry. The hydrodynamic coupling (HDC) combines the fast computational speed of the non-viscous potential flow model and the ability of reproducing overturning breaking wave crest of the viscous CFD model. This distinguishes the HDC approach to be advantageous and attractive for many engineering problems, especially when both large-scale wave propagation and local-scale wave breaking are important considerations. In this section, wave breakings over a submerged reef are simulated using both the potential flow approach and the HDC approach. The numerical setup follows the experiment at

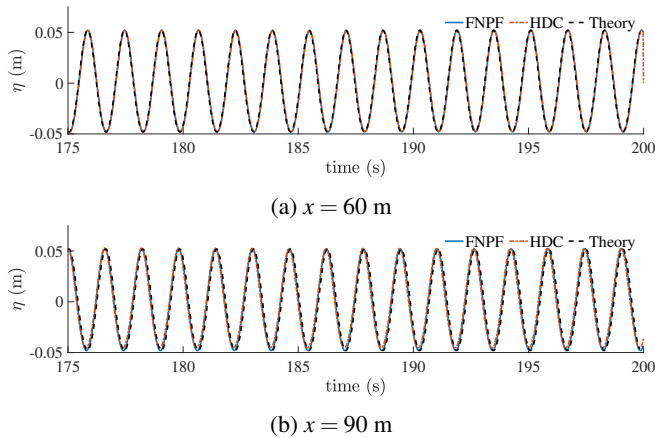


**FIGURE 3:** Comparison of the wave surface elevation time history in the simulation of wave propagation over constant water depth. (a) at  $x = 60$  m, (b) at  $x = 90$  m.

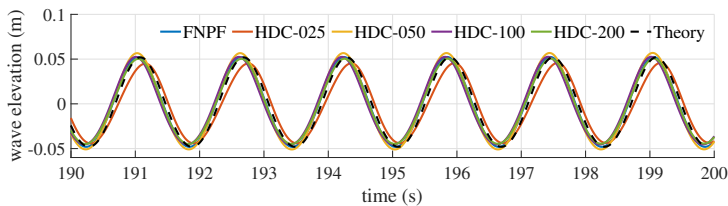


**FIGURE 4:** Comparison of free surface elevation time history in the simulations of regular wave propagation over constant water depth using different lengths of hydrodynamic coupling zone. HDC-025, HDC-050, HDC-100 and HDC-200 represent the cases with the lengths of hydrodynamic coupling zone equal to 0.25, 0.5, 1.0 and 2.0 wavelengths.

the Large Wave Flume (GWK), Hannover, Germany by Mo et al. [35] and Irschik et al. [17]. The longitudinal length of the numerical wave tank is 300 m, the water depth at the wave generation zone is 3.8 m. A submerged reef with a slope of 1:10 starts at 179 m from the wave generation one and rises up to 2.3 m at  $x = 201$  m, while remaining constant afterwards til the end of the numerical wave tank. In the potential flow FPNF domain, a wave generation zone is arranged at the inlet boundary and a numerical beach is arranged at the outlet boundary. The CFD domain starts at the coupling locations marked as  $X_c$  and a HDC zone is used to transfer the flow information from the potential flow domain to the CFD domain. The outlet boundary of the CFD domain stops at  $x = 210$  m, after the wave breaking take place. Here, an active absorption method is used at the outlet boundary to eliminate unwanted wave reflection at the shallow water region. The schematics of the numerical wave tank setup is shown in Fig. 5. In the first test, the coupling location is arranged to be ahead of the beginning of the underwater slope at  $X_c = 150$  m. The flow information at 50 s is used as input in the CFD domain. A horizontal cell size of 0.5 m is used in the FPNF domain, together with 15 cells in the vertical direction. The simulation of 140 s is finished in 106 s with 4 processors (2.7GHz Intel Xeon E5) using the potential flow model. In the CFD domain, a Cartesian grid with a uniform cell size of 0.05 m is used. For a duration of 50 s, the simulation is finished in 1.48 h with 12 processors the same as those used in the potential flow simulation.

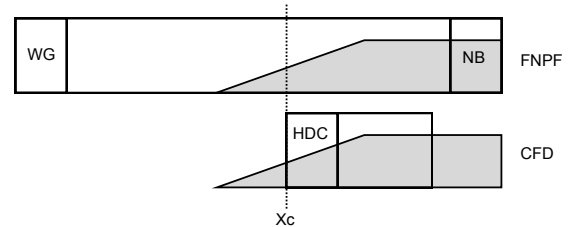


**FIGURE 5:** Schematics of the numerical wave tank set-up of the FPNF and the CFD domains for wave breaking over a submerged reef.

The simulated surface elevation time histories at several different locations on the slope are compared among the potential flow simulation, the hydrodynamic coupling simulation and the experimental measurements, as shown in Fig. 6. As can be seen, the time histories are generally in good agreement with each other both in terms of wave phase and amplitude. However, noticeable differences at the wave breaking location near  $x = 201$  m can be observed in Fig. 6c and the close-in view in Fig. 6d. First, the HDC simulation achieves an identical surface elevation with the experiment at the spilling breaker at  $t = 82.7$  s. The steep wave front is well preserved in the HDC model while the po-

tential flow model starts to dissipate energy slightly prematurely when the wave breaker is detected. More visible differences are seen at  $t = 90.3$  s where a plunging breaker takes place. Here, the HDC simulation captures a much steeper wave front that resembles the measurements, though a slightly lower crest height is observed due to the unstable nature of the wave breaker crest. The potential flow model predicts a similar wave crest height, but fails to represent the steep wave front. The time history shows that the HDC approach is much more appropriate for the study of slamming loads on structures.

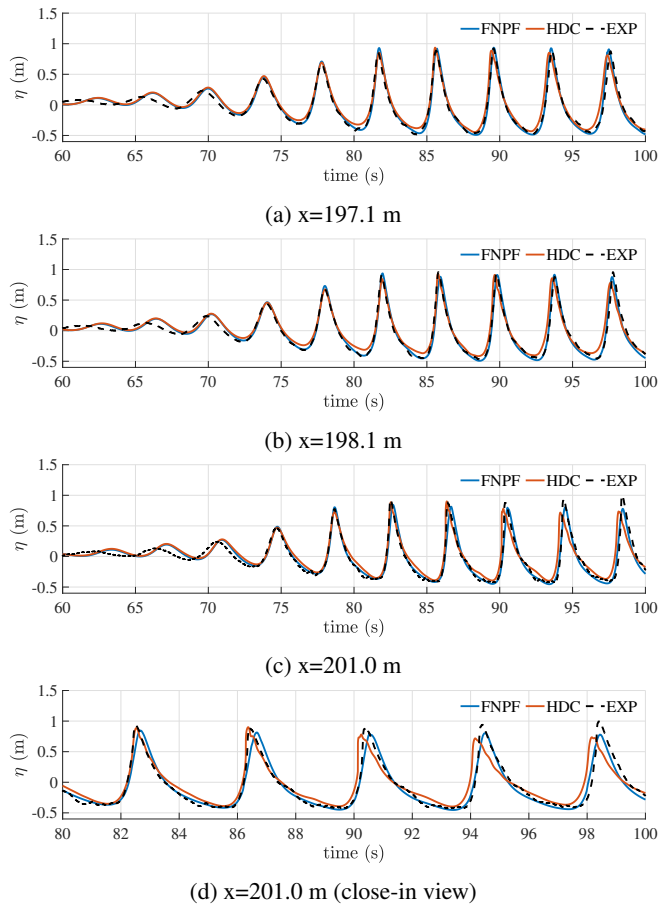


**FIGURE 6:** Comparison of the free surface elevation time history at different locations among REEF3D::FNPF, hydrodynamic coupling in REEF3D::CFD and experimental measurements for wave breaking over a submerged reef.

In order to confirm the wave breaking scenarios and demonstrate the complicated breaking wave crest geometry, the simulated wave fields from both the potential flow NWT and the HDC NWT are shown in Fig. 7 and Fig. 8 for  $t = 82.7$  s and  $t = 90.3$  s respectively. Here, significant differences are observed between

the two simulations. The steep wave front is well preserved and presented in Fig. 7b in comparison to Fig. 7a for the spilling wave breaker at  $t = 82.7$ . In Fig. 8, the plunging wave breaker with an over turning wave crest at  $t = 90.3$  is represented in the HDC simulation while the geometrical feature is lost in the potential flow simulation. The comparison confirms the wave breaking scenarios as can be derived from the surface elevations and reassures the advantage of the HDC approach for breaking wave simulations. The CFD domain is only between 150 m and 210 m in the current setup, which is only 1/5 of the entire experimental setup. As a result, the computational cost of the HDC approach is also nearly only 1/5 that of using the CFD simulation alone.

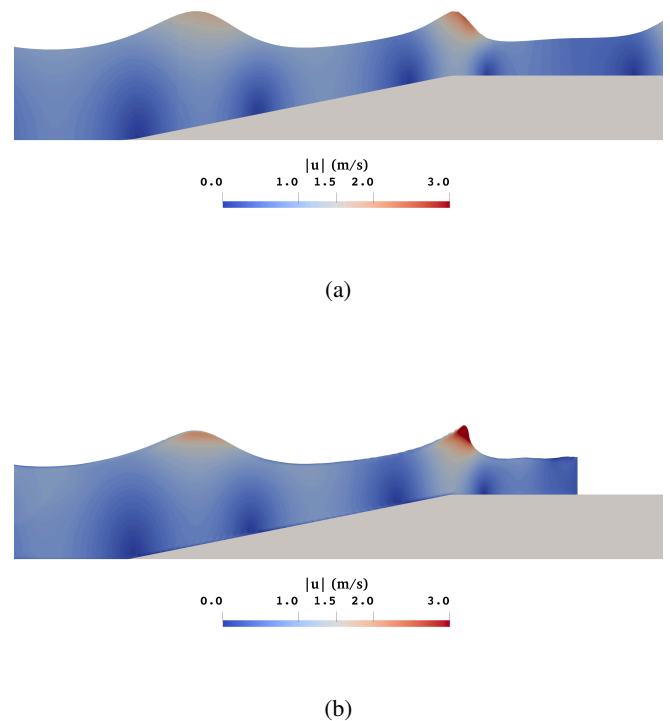
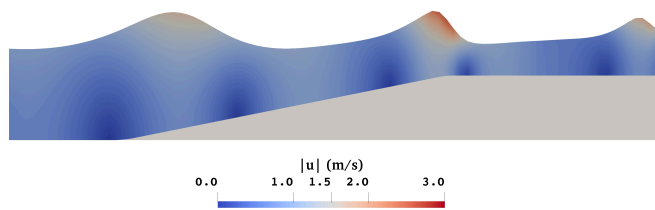
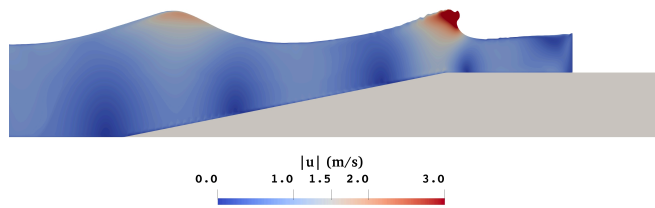


**FIGURE 7:** Spilling wave breaker at 82.7 s rendered with velocity magnitude in the simulations at (a) in REEF3D::FNPF domain and (b) in REEF3D::CFD domain.

However, it is also noted that the HDC approach is sensitive to the choice of the coupling locations. The numerical coupling needs to consider the critical wave events. If the coupling takes place too early, the advantage of minimising computational cost is reduced. If the numerical coupling takes place too late, the CFD domain might have received flow information after the crit-



(a)



(b)

**FIGURE 8:** Plunging wave breaker at 90.3 s rendered with velocity magnitude in the simulations at (a) in REEF3D::FNPF domain and (b) in REEF3D::CFD domain.

ical wave events, and thus lose the advantage of capturing the complicated viscous and turbulent wave phenomena. To demonstrate this effect, the HDC simulations with different coupling locations  $X_c = 150, 170$  and  $190$  m are used and the time histories at  $x = 201$  m are compared in Fig. 9. It is seen that the numerical simulations with  $X_c = 150$  and  $170$  m produce similar results and the steep wave fronts at breaking waves are represented. However, if the flow information is transferred to the CFD domain at  $X_c = 190$  m, the breaking waves are not well represented and the numerical results from the HDC approach are nearly identical as the potential flow simulation.

## CONCLUSION

The presented article describes the procedure to perform one-way hydrodynamic couplings (HDC) between a non-viscous fully nonlinear potential flow solver and a viscous CFD solver within the open-source hydrodynamic framework REEF3D. The velocities and free surface elevation from the potential flow solver on a  $\sigma$ -grid are transferred to the CFD domain as inputs.

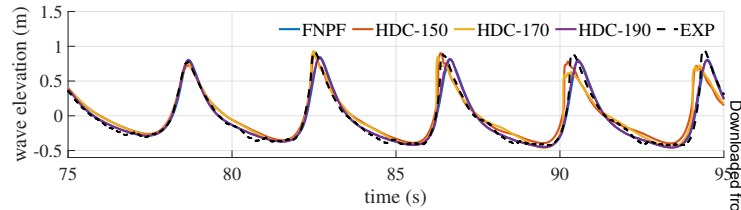


**FIGURE 9:** Free surface elevation time history at  $x = 201.0$  m with different hydrodynamic coupling locations for wave breaking scenarios over a submerged reef.

The grid generator DIVEMesh in the REEF3D framework interpolates the flow information into Cartesian grid in the CFD domain and re-decomposes the computational domain to allow parallel computations with different numbers of processors in the non-viscous and viscous models. A relaxation method is used to initialise the flow information from the potential flow domain and propagate the waves in the CFD domain.

The study of wave propagation over a constant water depth proves the effectiveness and accuracy of the presented HDC method. It also shows the sensitivity of the coupling zone length on the quality of the wave field in the CFD domain. The study on wave breaking over a submerged reef confirms the advantage of the HDC approach by combining the computational efficiency of the non-viscous potential flow solver and the ability to represent strong overturning breaking waves of the viscous CFD solver.

In general, the presented HDC approach within REEF3D is seen to be effective and accurate. In the future, high-order interpolation methods are to be explored to further increase the flexibility and accuracy at the coupling boundary.

## REFERENCES

- [1] Jacobsen, N. G., Fuhrman, D. R., and Fredsøe, J., 2012. “A wave generation toolbox for the open-source CFD library: OpenFOAM”. *International Journal for Numerical Methods in Fluids*, **70**(9), pp. 1073–1088.
- [2] Higuera, P., Lara, L. J., and Losada, I. J., 2013. “Realistic wave generation and active wave absorption for Navier-Stokes models application to OpenFOAM”. *Coastal Engineering*, **71**, pp. 102–118.
- [3] Westphalen, J., Greaves, D. M., Williams, C. J. K., Hunt-Raby, A., and J., Z., 2012. “Focused waves and wave-structure interaction in a numerical wave tank”. *Ocean engineering*, **45**, pp. 9–21.
- [4] Pakozdi, C., Kendon, T. E., and Stansberg, C. T., 2012. “A numerical study of a focused wave packet near the surf zone”. *OMAE 2012, 31st International Conference on Ocean, Offshore & Arctic Engineering, Rio de Janeiro, Brazil*.
- [5] Bihs, H., Kamath, A., Alagan Chella, M., Aggarwal, A.,



- and Arntsen, Ø. A., 2016. “A new level set numerical wave tank with improved density interpolation for complex wave hydrodynamics”. *Computers & Fluids*, **140**, pp. 191–208.
- [6] Alagan Chella, M., Bihs, H., and D., M., 2019. “Numerical modeling of breaking wave kinematics and wave impact pressures on a vertical slender cylinder,”. *Journal of Fluids and Structures*, **86**, pp. 94–123.
- [7] Aggarwal, A., Bihs, H., Shirinov, S., and Myrhaug, D., 2019. “Estimation of breaking wave properties and their interaction with a jacket structure”. *Journal of Fluids and Structures*, **91**, p. 102722.
- [8] Kamath, A., and Bihs, H., 2017. “Study of water impact and entry of a free falling wedge using computational fluid dynamics simulations”. *Journal of Offshore Mechanics and Arctic Engineering*, **139**, pp. 031802–1.
- [9] Engsig-Karup, A., Bingham, H., and Lindberg, O., 2009. “An efficient flexible-order model for 3D nonlinear water waves”. *Journal of Computational Physics*, **228**, pp. 2100–2118.
- [10] Engsig-Karup, A. P., Madsen, M. G., and Glimberg, S. L., 2012. “A massively parallel gpu-accelerated model for analysis of fully nonlinear free surface waves”. *International Journal for Numerical Methods in Fluids*, **70**(1).
- [11] Engsig-Karup, A. P., Eskilsson, C., and Bigoni, D., 2016. “A stabilised nodal spectral element method for fully nonlinear water waves”. *Journal of Computational Physics*, **318**, pp. 1–21.
- [12] Li, B., and Fleming, C. A., 1997. “A three dimensional multigrid model for fully nonlinear water waves”. *Coastal Engineering*, **30**, pp. 235–258.
- [13] Bihs, H., Wang, W., Pakozdi, C., and Kamath, A., 2020. “Reef3d::fnpf – a flexible fully nonlinear potential flow solver”. *Journal of Offshore Mechanics and Arctic Engineering*.
- [14] Wang, W., Kamath, A., Pakozdi, C., and Bihs, H., 2019. “Investigation of focusing wave properties in a numerical wave tank with a fully nonlinear potential flow model”. *Journal of Marine Science and Engineering*, **7**(375).
- [15] Paulsen, B. T., Bredmose, H., and Bingham, H. B., 2014. “An efficient domain decomposition strategy for wave loads on surface piercing circular cylinders”. *Coastal Engineering*, **86**, pp. 57–76.
- [16] Baquet, A., Kim, J., and Huang, Z. J., 2017. “Numerical modeling using cfd and potential wave theory for three-hour nonlinear irregular wave simulations”. *36th International Conference on Ocean, Offshore and Arctic Engineering, OMAE, Trondheim, Norway*.
- [17] Irschik, K., Sparboom, U., and Oumeraci, H., 2002. “Breaking wave characteristics for the loading of a slender pile”. In Proc. *28th International Conference on Coastal Engineering*, Cardiff, Wales.
- [18] van der Vorst, H., 1992. “BiCGStab: A fast and smoothly converging variant of Bi-CG for the solution of nonsymmetric linear systems”. *SIAM Journal on Scientific and Statistical Computing*, **13**, pp. 631–644.
- [19] Ashby, S. F., and Flagout, R. D., 1996. “A parallel multigrid preconditioned conjugate gradient algorithm for groundwater flow simulations”. *Nuclear Science and Engineering*, **124**(1), pp. 145–159.
- [20] Mayer, S., Garapon, A., and Sørensen, L. S., 1998. “A fractional step method for unsteady free surface flow with applications to non-linear wave dynamics”. *International Journal for Numerical Methods in Fluids*, **28**, pp. 293–315.
- [21] Chen, Q., Kelly, D. M., and Zang, J., 2019. “On the relaxation approach for wave absorption in numerical wave tanks”. *Ocean Engineering*, **187**, p. 106210.
- [22] Schäffer, H. A., and Klopman, G., 2000. “Review of multidirectional active wave absorption methods”. *Journal of Waterway, Port, Coastal, and Ocean Engineering*, **126**(2), pp. 88–97.
- [23] Jiang, G. S., and Shu, C. W., 1996. “Efficient implementation of weighted ENO schemes”. *Journal of Computational Physics*, **126**, pp. 202–228.
- [24] Shu, C. W., and Osher, S., 1988. “Efficient implementation of essentially non-oscillatory shock capturing schemes”. *Journal of Computational Physics*, **77**, pp. 439–471.
- [25] Wilcox, D. C., 1994. *Turbulence modeling for CFD*. DCW Industries Inc., La Canada, California.
- [26] Naot, D., and Rodi, W., 1982. “Calculation of secondary currents in channel flow”. *Journal of the Hydraulic Division, ASCE*, **108**(8), pp. 948–968.
- [27] Kamath, A., Fleit, G., and Bihs, H., 2019. “Investigation of free surface turbulence damping in rans simulations for complex free surface flows”. *Water*, **11**(456), pp. 1–26.
- [28] Hossain, M. S., and Rodi, W., 1980. “Mathematical modeling of vertical mixing in stratified channel flow”. In Proc., *2nd Symposium on Stratified Flows*, Trondheim, Norway.
- [29] Chorin, A., 1968. “Numerical solution of the Navier-Stokes equations”. *Mathematics of Computation*, **22**, pp. 745–762.
- [30] Berthelsen, P. A., and Faltinsen, O. M., 2008. “A local directional ghost cell approach for incompressible viscous flow problems with irregular boundaries”. *Journal of Computational Physics*, **227**, pp. 4354–4397.
- [31] Osher, S., and Sethian, J. A., 1988. “Fronts propagating with curvature-dependent speed: algorithms based on Hamilton-Jacobi formulations”. *Journal of Computational Physics*, **79**, pp. 12–49.
- [32] Jiang, G. S., and Peng, D., 2000. “Weighted ENO schemes for Hamilton-Jacobi equations”. *SIAM Journal on Scientific Computing*, **21**, pp. 2126–2143.
- [33] Sussman, M., Smereka, P., and Osher, S., 1994. “A level set approach for computing solutions to incompressible two-

- phase flow”. *Journal of Computational Physics*, **114**, pp. 146–159.
- [34] Peng, D., Merriman, B., Osher, S., Zhao, H., and Kang, M., 1999. “A PDE-based fast local level set method”. *Journal of Computational Physics*, **155**, pp. 410–438.
- [35] Mo, W., Irschik, K., Oumeraci, H., and Liu, P., 2007. “A 3D numerical model for computing non-breaking wave forces on slender piles”. *Journal of Engineering Mathematics*, **58**, pp. 19–30.